ISSN 1063-7834, Physics of the Solid State, 2018, Vol. 60, No. 10, pp. 1989–1998. © Pleiades Publishing, Ltd., 2018.
Original Russian Text © I.A. Gudim, A.A. Demidov, E.V. Eremin, D.K. Shukla, 2018, published in Fizika Tverdogo Tela, 2018, Vol. 60, No. 10, pp. 1947–1956.

MAGNETISM

Magnetic and Magnetodielectric Properties of $Ho_{0.5}Nd_{0.5}Fe_3(BO_3)_4$

I. A. Gudim[a], A. A. Demidov[b, *], E. V. Eremin[a, c], and D. K. Shukla[d]

[a] *Kirensky Institute of Physics, Krasnoyarsk Scientific Center, Siberian Branch, Russian Academy of Sciences, Krasnoyarsk, 660036 Russia*

[b] *Bryansk State Technical University, Bryansk, 241035 Russia*

[c] *Siberian State University of Science and Technology, Krasnoyarsk, 660014 Russia*

[d] *UGC-DAE Consortium for Scientific Research, Indore, 452017 India*

**e-mail: demandr@yandex.ru*

Received April 12, 2018

Abstract—The magnetic and magnetodielectric properties of $Ho_{0.5}Nd_{0.5}Fe_3(BO_3)_4$ ferroborate with the competing Ho–Fe and Nd–Fe exchange couplings have been experimentally and theoretically investigated. Step anomalies in the magnetization curves at the spin-reorientation transition induced by the magnetic field $\mathbf{B} \parallel \mathbf{c}$ have been found. The spontaneous spin-reorientation transition temperature $T_{SR} \approx 8$ K has been refined. The measured magnetic properties and observed features are interpreted using a single theoretical approach based on the molecular field approximation and calculations within the crystal field model of the rare-earth ion. Interpretation of the experimental data includes determination of the crystal field parameters for Ho^{3+} and Nd^{3+} ions in $Ho_{0.5}Nd_{0.5}Fe_3(BO_3)_4$ and parameters of the Ho–Fe and Nd–Fe exchange couplings.

DOI: 10.1134/S1063783418100086

1. INTRODUCTION

The rare-earth borates $RM_3(BO_3)_4$ (R = Y or La–Lu and M = Al, Sc, Cr, Fe, and Ga) exhibit a vast diversity of magnetic, magnetoelectric, magnetoelastic, and other physical properties [1–5]. Borates with two magnetic subsystems ($RFe_3(BO_3)_4$ ferroborates) are multiferroics [1, 3, 4]. It has been recently established that $RAl_3(BO_3)_4$ alumoborates known for their nonlinear-optical properties exhibit giant magnetoelectric polarization [5]. An increased interest in the $RM_3(BO_3)_4$ borates is due to the possibility of studying the substituted $R_{1-x}R'_xFe_3(BO_3)_4$ compositions, where the presence of competing R–Fe and R'–Fe exchange couplings can ensure the occurrence of spontaneous reorientation transitions [3, 6, 7].

The R ions suitable for synthesis and study of a substituted ferroborate with the competing exchange couplings are Ho^{3+} and Nd^{3+} ions. The iron magnetic moments in $HoFe_3(BO_3)_4$ are antiferromagnetically ordered at $T_N \approx 38$–39 K and, with a decrease in temperature to $T_{SR} \approx 4.7$–5 K, lie in the *ab* basal plane, similar to the magnetic moments of Ho^{3+} ions [3, 8, 9]. At $T_{SR} \approx 4.7$–5 K, the spontaneous spin-reorientation transition occurs; as a result, the magnetic moments of the Ho and Fe subsystems align parallel to the *c* axis. In $NdFe_3(BO_3)_4$ at $T < T_N \approx 31$ K, all magnetic moments lie in the *ab* basal plane [4, 10]. $YFe_3(BO_3)_4$ at $T < T_N \approx 37$–38 K also has an easy-plane (EP) magnetic structure [4, 8, 11]. Thus, the competition of contributions of the Ho, Nd, and Fe subsystems to the magnetic anisotropy of $Ho_{1-x}Nd_xFe_3(BO_3)_4$ can result in the occurrence of the spontaneous and magnetic field-induced spin-reorientation transitions. These transitions were observed for the $Ho_{1-x}Nd_xFe_3(BO_3)_4$ compositions with $x = 0.5$ [3] and 0.75 [12].

It seemed obvious that substitution of Nd^{3+} ions stabilizing the EP state for Ho^{3+} ions in $Ho_{1-x}Nd_xFe_3(BO_3)_4$ should shift the temperature of spin-reorientation transition from the EP to easy-axis (EA) state from a value of $T_{SR} \approx 4.7$–5 K found in $HoFe_3(BO_3)_4$ to the lower-temperature region. However, in $Ho_{0.5}Nd_{0.5}Fe_3(BO_3)_4$, the temperature T_{SR} unexpectedly increased to 9 K [3] and in $Ho_{0.25}Nd_{0.75}Fe_3(BO_3)_4$, the T_{SR} value remained the same as in $HoFe_3(BO_3)_4$ [12]. This clearly demonstrates that the simple summation of the contributions of the EA and EP subsystems in the substituted compound cannot explain the processes occurring in the resulting magnetic structure. As was shown in [13], the increase in T_{SR} in $Ho_{0.5}Nd_{0.5}Fe_3(BO_3)_4$ as compared with $HoFe_3(BO_3)_4$ is caused by broadening of the temperature range of the stable initial low-temperature state of the magnetic subsystem due to its change from the EA (as in $HoFe_3(BO_3)_4$) to the angular state.

This work continues the investigations of the $Ho_{0.5}Nd_{0.5}Fe_3(BO_3)_4$ ferroborate and presents the

results of experimental and theoretical study of the magnetization and magnetic susceptibility curves and field and temperature dependences of the permittivity and specific heat. New experimental data on the $Ho_{0.5}Nd_{0.5}Fe_3(BO_3)_4$ ferroborate are reported and discussed, including the field and temperature dependences of the permittivity $\varepsilon_a(B_a, T)$, magnetization curves $M_{c,\perp c}(B)$, and susceptibility curves $\chi_{c,\perp c}(T)$ at $T = 20$–300 K and $\chi_c(T)$ at $T = 2$–300 K for $B = 0.1$ T.

2. EXPERIMENTAL

The $Ho_{0.5}Nd_{0.5}Fe_3(BO_3)_4$ single crystals were grown from fluxes based on bismuth thimolybdate 82 wt % [$Bi_2Mo_3O_{12}$ + $3B_2O_3$ + $0.25Ho_2O_3$ + $0.25Nd_2O_3$] + 18 wt % $Ho_{0.5}Nd_{0.5}Fe_3(BO_3)_4$ by the technique described in detail in [14, 15]. The saturation temperature T_{sat} was determined accurate to ±3°C using reference crystals preliminary synthesized by spontaneous nucleation. In addition, crystals ~1 mm in size were grown in the spontaneous nucleation regime at a temperature of $T = T_{sat} - 20$°C. These crystals were then used as seeds for growing crystals about $5 \times 7 \times 7$ mm^3 in size. When growing crystals on seeds, a starting temperature of $T = T_{sat} - 7$°C was specified, which approximately corresponded to the middle of the flux metastability region. After that, the flux temperature was decreased with a step of 0.1°C, according to the program with increasing rate, so that the crystal growth rate was no higher than 1 mm per day. In this case, a crystal holder with seeds rotated at a speed of 30–40 rpm and a reverse period of 1 min. After finishing the growth process (in 10–15 days), the crystal holder was raised above the flux and a furnace was cooled to room temperature at the switched-off power. The obtained samples had good optical quality and contained no visible defects.

The magnetic measurements were performed on a Quantum Design Physical Property Measurement System in the temperature range of 2–300 K and magnetic fields of up to 9 T. The permittivity was investigated by measuring the capacitance with an Agilent E4980A Precision LCR Meter in frequency range from 10 kHz to 2 MHz.

3. CALCULATION TECHNIQUE

In the calculations, we used a theoretical approach successfully applied earlier to studying pure $RFe_3(BO_3)_4$ (R = Tb [2], Nd [16], and Ho [17]) ferroborates and substituted $Nd_{1-x}Dy_xFe_3(BO_3)_4$ [7] and $Sm_{0.7}Ho_{0.3}Fe_3(BO_3)_4$ [18] compositions. This theoretical approach is based on a crystal field (CF) model of the R ion and molecular field approximation. Both the rare-earth (holmium and neodymium) and iron magnetic subsystems interacting with each other are responsible for the magnetic properties of $Ho_{1-x}Nd_xFe_3(BO_3)_4$. The interaction within the R subsystem can be ignored. The iron subsystem can be considered as a set of two antiferromagnetic sublattices. The R subsystem magnetized by the *f*–*d* coupling can also be presented in the form of two sublattices. According to the $Ho_{1-x}Nd_xFe_3(BO_3)_4$ magnetic structure and coupling hierarchy, the effective Hamiltonians of Fe and R (Ho and Nd) ions of the *i*th ($i = 1, 2$) sublattices in magnetic field **B** can be written as

$$\mathcal{H}_i(\mathrm{R}) = \mathcal{H}_i^{\mathrm{CF}} + g_J^{\mathrm{R}}\mu_{\mathrm{B}}\mathbf{J}_i^{\mathrm{R}}[\mathbf{B} + \lambda_{fd}^{\mathrm{R}}\mathbf{M}_i^{\mathrm{Fe}}], \quad (1)$$

$$\mathcal{H}_i(\mathrm{Fe}) = g_S\mu_{\mathrm{B}}\mathbf{S}_i[\mathbf{B} + \lambda\mathbf{M}_j^{\mathrm{Fe}} + (1-x)\lambda_{fd}^{\mathrm{Ho}}\mathbf{m}_i^{\mathrm{Ho}} + x\lambda_{fd}^{\mathrm{Nd}}\mathbf{m}_i^{\mathrm{Nd}}], \quad j = 1, 2, \quad j \neq i. \quad (2)$$

Here, $\mathcal{H}_i^{\mathrm{CF}}$ is the CF Hamiltonian, g_J^{R} is the Lande factor, $\mathbf{J}_i^{\mathrm{R}}$ is the operator of R-ion angular momentum, $g_S = 2$ is the *g* factor, $\mathbf{S}_i$ is the operator of the spin angular momentum of the iron ion, and $\lambda_{fd}^{\mathrm{R}} < 0$ are the molecular constants of the R–Fe and Fe–Fe antiferromagnetic couplings.

The magnetic moments of the *i*th iron ($\mathbf{M}_i^{\mathrm{Fe}}$) and rare-earth ($\mathbf{m}_i^{\mathrm{R}}$) sublattices per formula unit are determined by the relations

$$\mathbf{M}_i^{\mathrm{Fe}} = -3g_S\mu_{\mathrm{B}}\langle\mathbf{S}_i\rangle, \quad \mathbf{m}_i^{\mathrm{R}} = -g_J^{\mathrm{R}}\mu_{\mathrm{B}}\langle\mathbf{J}_i^{\mathrm{R}}\rangle. \quad (3)$$

The expression for the CF Hamiltonian in the irreducible tensor operators has the form

$$\mathcal{H}^{\mathrm{CF}} = B_0^2C_0^2 + B_0^4C_0^4 + B_3^4(C_{-3}^4 - C_3^4) + B_0^6C_0^6 + B_3^6(C_{-3}^6 - C_3^6) + B_6^6(C_{-6}^6 + C_6^6). \quad (4)$$

The CF parameters B_q^k for the Ho^{3+} and Nd^{3+} ions in $Ho_{1-x}Nd_xFe_3(BO_3)_4$ are unknown. In addition, there has been a lack of data on splitting of the lower levels of the main multiplet of Ho^{3+} and Nd^{3+} ions in $Ho_{1-x}Nd_xFe_3(BO_3)_4$.

The calculation of the values and directions of the magnetic moments of the Fe and R subsystems by solving self-consistent problems on the basis of Hamiltonians (1), (2) under the minimum thermodynamic potential conditions makes it possible to determine the regions of stability of different magnetic phases, phase transition fields, magnetization curves, susceptibility, etc. The $Ho_{1-x}Nd_xFe_3(BO_3)_4$ thermodynamic potential was previously presented by us in [13].

The energy of anisotropy of the *i*th sublattice of the Fe subsystem has the form

$$\Phi_{\mathrm{an}}^i = K_2^{\mathrm{Fe}}\sin^2\vartheta_i + K_4^{\mathrm{Fe}}\sin^4\vartheta_i + K_{66}^{\mathrm{Fe}}\sin^6\vartheta_i\cos 6\varphi_i, \quad (5)$$

where the anisotropy constant $K_2^{\mathrm{Fe}} < 0$ stabilizes the EP state, $K_4^{\mathrm{Fe}} > 0$ is the EA state, $K_{66}^{\mathrm{Fe}} < 0$ is the anisot-

ropy constant in the *ab* basal plane, and ϑ_i and φ_i are the polar and azimuth angles of the deviation of iron magnetic moment vector $\mathbf{M}_i^{\mathrm{Fe}}$ from the *c* and *a* axes, respectively.

The $Ho_{1-x}Nd_xFe_3(BO_3)_4$ magnetization and susceptibility are

$$\mathbf{M} = \frac{1}{2}\sum_i^2 (\mathbf{M}_i^{\mathrm{Fe}} + (1-x)\mathbf{m}_i^{\mathrm{Ho}} + x\mathbf{m}_i^{\mathrm{Nd}}),$$
$$\chi_k = \chi_k^{\mathrm{Fe}} + (1-x)\chi_k^{\mathrm{Ho}} + x\chi_k^{\mathrm{Nd}}, \quad k = a,b,c. \tag{6}$$

In the ordered phase, the initial magnetic susceptibilities of the compound can be determined from the initial linear portions of the magnetization curves calculated for the corresponding external magnetic field directions. In the paramagnetic region, the susceptibility of the R subsystem was calculated from the well-known Van Vleck formula using the energy spectrum and wave functions calculated on the basis of Hamiltonian (4). The susceptibility of the Fe subsystem can be described by the Curie–Weiss law with the corresponding paramagnetic Néel temperature Θ.

The contribution of the R subsystem to the magnetic part of $Ho_{1-x}Nd_xFe_3(BO_3)_4$ specific heat was calculated using the formula (per formula unit)

$$C = (1-x)C_{\mathrm{Ho}} + xC_{\mathrm{Nd}}, \quad C_{\mathrm{R}} = k_{\mathrm{B}}\frac{\langle E^2\rangle - \langle E\rangle^2}{(k_{\mathrm{B}}T)^2}. \tag{7}$$

The thermal means $\langle E^2\rangle$ and $\langle E\rangle^2$ were calculated using the R-ion spectrum formed by the CF and interactions with the Fe subsystem and external magnetic field.

4. RESULTS AND DISCUSSION

As is known, ferroborates with a small ionic radius of the R ion, in particular, $HoFe_3(BO_3)_4$, undergo the structural phase transition at which the local symmetry of the R ion decreases from D_3 (at $T > T_S$) to C_2 (at $T < T_S$) [4]. In $NdFe_3(BO_3)_4$, this transition does not occur [4]. Since the main features of the low-temperature magnetic properties of $HoFe_3(BO_3)_4$ can be described in the high-temperature D_3 symmetry [17], the experimental data on $Ho_{0.5}Nd_{0.5}Fe_3(BO_3)_4$ were also described in this symmetry [13], for which the CF Hamiltonian has a simpler form. Recent study of the $Ho_{0.5}Nd_{0.5}Fe_3(BO_3)_4$ infrared absorption spectra in the spectral range of 30–1700 cm^{-1} at $T = 6$–300 K [19] showed no variations that would be related to the structural phase transitions. Thus, in the absence of experimental data on a structural transition in $Ho_{0.5}Nd_{0.5}Fe_3(BO_3)_4$, the absence of this transition in $NdFe_3(BO_3)_4$, and the lack of data on splittings of the lower levels in the main multiplets of Ho^{3+} and Nd^{3+} ions in $Ho_{0.5}Nd_{0.5}Fe_3(BO_3)_4$, taking into account that the magnetic properties of $HoFe_3(BO_3)_4$ [17] and $Ho_{0.5}Nd_{0.5}Fe_3(BO_3)_4$ [13] can be described in the D_3 symmetry, we described our new experimental data on $Ho_{0.5}Nd_{0.5}Fe_3(BO_3)_4$ in the D_3 symmetry. This approximation allowed us to significantly reduce the number of parameters used in calculating the initially unknown CF parameters (from 15 for the C_2 symmetry to 6 for the D_3 symmetry); however, in the case of detecting a structural transition, the obtained calculated data should only be qualitatively recognized.

Study of the ratio between the contributions of the $Ho_{0.5}$ and $Nd_{0.5}$ subsystems to the resulting magnetic characteristics of $Ho_{0.5}Nd_{0.5}Fe_3(BO_3)_4$ showed that, e.g., at $T = 2$ K and $B_{c,\perp c} = 9$ T, the Ho subsystem contribution is ~84.7% to the magnetization $M_c(B)$ and ~82.8% to $M_{\perp c}(B)$. The sensitivity to the variations in the CF parameters for Ho^{3+} ions is also higher than that for Nd^{3+} ions. The calculations revealed no significant improvement in describing the magnetization $M_{c,\perp c}(B)$, susceptibility $\chi_{c,\perp c}(T)$, and specific heat $C_p/T(T)$ curves of $Ho_{0.5}Nd_{0.5}Fe_3(BO_3)_4$ when using different and identical sets of CF parameters for the Ho and Nd subsystems. Therefore, a single set of parameters for the Ho and Nd subsystems was used in the calculations.

The experimental magnetization curves $M_{c,\perp c}(B)$ in fields of up to 9 T, temperature dependences of the initial magnetic susceptibility $\chi_{c,\perp c}(T)$, and specific heat $C_p/T(T)$ from study [3] were used by us to determine the CF parameters. The initial values of the CF parameters, with which the procedure of minimizing the corresponding objective function started, were chosen to be the previously found parameters for $HoFe_3(BO_3)_4$ [17] and $NdFe_3(BO_3)_4$ [16]. In addition, the set of CF parameters found by us previously when describing of only the susceptibility and specific heat curves for $Ho_{0.5}Nd_{0.5}Fe_3(BO_3)_4$ was taken as initial one [13]. It was established that the best description of the entire set of experimental characteristics is obtained with the use of parameters (cm^{-1})

$$B_0^2 = 410, \quad B_0^4 = -1250, \quad B_3^4 = 870, \quad B_0^6 = 350,$$
$$B_3^6 = 110, \quad B_6^6 = 150. \tag{8}$$

The set of CF parameters (8) corresponds to the energies of eight lower Stark levels of the main multiplets of Ho^{3+} and Nd^{3+} ions in $Ho_{0.5}Nd_{0.5}Fe_3(BO_3)_4$ at $B = 0$ (see Table 1): at $T > T_N$, taking into account the *f*–*d* coupling at $T = 10$ K $> T_{SR}$ (the EP state) and $T = 2$ K $< T_{SR}$ (the general angular state). It can be seen that at $T < T_N$, the account for the *f*–*d* interaction leads to elimination of the degeneracy of the energy levels. At T_{SR}, the energy levels shift relative to each other and their splittings change: in Ho, which stabilizes the EA state, the splitting of the lower levels increases from $\Delta_{fd} \approx 2.2$ to 10.9 cm^{-1} and in Nd, which

Table 1. Energies of the eight lower levels of the main multiplets of Ho^{3+} and Nd^{3+} ions in $Ho_{0.5}Nd_{0.5}Fe_3(BO_3)_4$ split by the crystal field and with regard to the *f–d* coupling at $B = 0$ in the paramagnetic and ordered temperature regions

R	T	$\Delta = E_i - E_1$, cm^{-1} ($i = 1–8$)
Ho	$T > T_N$	0, 0, 12.5, 12.5, 16.9, 38, 152.6, 178.7
	10 K > T_{SR}	0, 2.2, 17.9, 19.8, 29.3, 46.4, 156.6,182.8
	2 K < T_{SR}	0, 10.9, 19.3, 25.9, 30.8, 51.4, 160.7, 179.4
Nd	$T > T_N$	0, 0, 39.7, 39.7, 48.6, 48.6, 202.6, 202.6
	10 K > T_{SR}	0, 7.5, 44.2, 44.2, 50.5, 56, 207, 207
	2 K < T_{SR}	0, 7.3, 39.1, 48, 50.1, 57.5, 202, 212

stabilizes the EP state, the levels slightly narrow from $\Delta_{fd} \approx 7.5$ to 7.3 cm^{-1}.

The magnetic characteristics presented below were calculated for the parameters given in Table 2 together (for comparison) with the parameters for $HoFe_3(BO_3)_4$ and $NdFe_3(BO_3)_4$. In addition, we used in the calculations the uniaxial anisotropy constants of the Fe subsystem ($K_2^{Fe} = -2.85$ T μ_B and $K_4^{Fe} = 0.55$ T μ_B at $T = 4.2$ K) and the iron anisotropy constant in the basal plane ($K_{66}^{Fe} = -1.35 \times 10^{-2}$ Tμ_B [16]). The K_2^{Fe} and K_4^{Fe} values are consistent with the corresponding uniaxial constants determined when describing the angular state in $Pr_xY_{1-x}Fe_3(BO_3)_4$ [22] and results of investigation of the antiferromagnetic resonance in $YFe_3(BO_3)_4$ [23], according to which the effective anisotropy field at the exchange field $H_E = 55$ T for the Fe subsystems will be $H_A^{Fe} = 0.183$ T; therefore, for $M^{Fe} = 3 \times 5\mu_B$, we have the constant $K_2^{Fe} = -2.75$ T μ_B.

To calculate the magnetic characteristics of $Ho_{0.5}Nd_{0.5}Fe_3(BO_3)_4$ in the external magnetic fields directed parallel and perpendicular to the trigonal *c* axis, we used the schemes of orientations of the magnetic moments of iron ($\mathbf{M}_i^{Fe}$) and rare earth element $\mathbf{m}_i = \mathbf{m}_i^{Nd_{0.5}} + \mathbf{m}_i^{Dy_{0.5}}$ from Fig. 1.

Figure 2 shows the experimental $Ho_{0.5}Nd_{0.5}Fe_3(BO_3)_4$ magnetization curves $M_{c,\perp c}(B)$

Table 2. Parameters of $Ho_{0.5}Nd_{0.5}Fe_3(BO_3)_4$ and, for comparison, $HoFe_3(BO_3)_4$ [20] and $NdFe_3(BO_3)_4$ [16]: B_{dd1} (intra-chain Fe–Fe), B_{dd2} (inter-chain Fe–Fe), and B_{fd} are the low-temperature values of exchange fields corresponding to the molecular constants λ_1, λ_2, and λ_{fd}; $M_0 = |M_i(T = 0, B = 0)| = 15\mu_B$ is the iron magnetic moment per formula unit; Δ_{fd} is the low-temperature splitting of the R-ion ground state due to the *f–d* coupling (in the angular (ANG), EA, and EP states); T_{SR} is the spin-reorientation transition temperature; θ_1 is the angle of deviation of $\mathbf{M}_1^{Fe}$ from the *c* axis; T_N is the Néel temperature; and Θ is the paramagnetic Néel temperature for the Fe subsystem

Compound	$HoFe_3(BO_3)_4$	$Ho_{0.5}Nd_{0.5}Fe_3(BO_3)_4$		$NdFe_3(BO_3)_4$
$B_{dd1} = \lambda_1 M_0$, T	68	55		58
λ_1, T/μ_B	−4.53	−3.67		−3.87
$B_{dd2} = \lambda_2 M_0$, T	26	28		27
λ_2, T/μ_B	−1.73	−1.87		−1.8
$B_{fd} = \lambda_{fd} M_0$, T	3.49	3.7 (Ho) 7.3 (Nd)		7.1
λ_{fd}, T/μ_B	−0.23	−0.25 (Ho) −0.49 (Nd)		−0.47
$\Delta_{fd} = \mu_B g\lvert\lambda_{fd}\rvert M_0$, cm^{-1}	~10.6 (EA)	Ho	~10.9 (ANG) ~2.2 (EP)	8.8 (EP)
	~9.7 (EP)	Nd	~7.3 (ANG) ~7.5 (EP)	
T_{SR}, K	~4.7–5 [3, 8, 21]	~8 ~9 [3]		
θ_1, deg ($B = 0$)	0 ($T < T_{SR}$) 90 ($T > T_{SR}$)	~46.8 ($T = 2$ K < T_{SR}) 90 ($T > T_{SR}$)		90
T_N, K	~37.4–39 [3, 8, 21]	~32 ~32 [3]		~31 [4]
Θ, K	−210	−120		−130

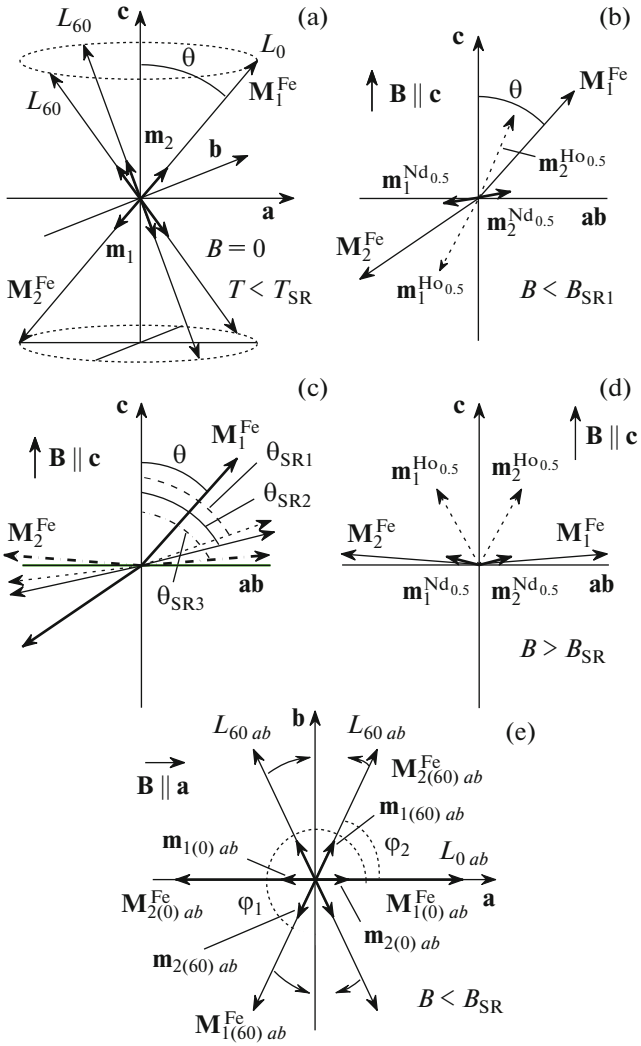

Fig. 1. Schemes of orientations of the iron and rare-earth magnetic moments $\mathbf{M}_i^{Fe}$ and $\mathbf{m}_i = \mathbf{m}_i^{Ho_{0.5}} + \mathbf{m}_i^{Nd_{0.5}}$ used in the calculation of the magnetic characteristics of $Ho_{0.5}Nd_{0.5}Fe_3(BO_3)_4$. Scheme *a*: the angular state at $B = 0$ (easy magnetization axes cone). Schemes *b*, *c*, and *d*: at $\mathbf{B} \parallel \mathbf{c}$ (the *ab* plane is perpendicular to the figure plane). Scheme *e*: $\mathbf{B} \perp \mathbf{c}$ (the *c* axis is perpendicular to the figure plane). Projections of the magnetic moments onto the *ab* plane in domains with the antiferromagnetic axes at angles $\varphi_i = 0(L_0)$ and $\varphi_i = \pm 60°(L_{60})$ to the *a* axis are shown.

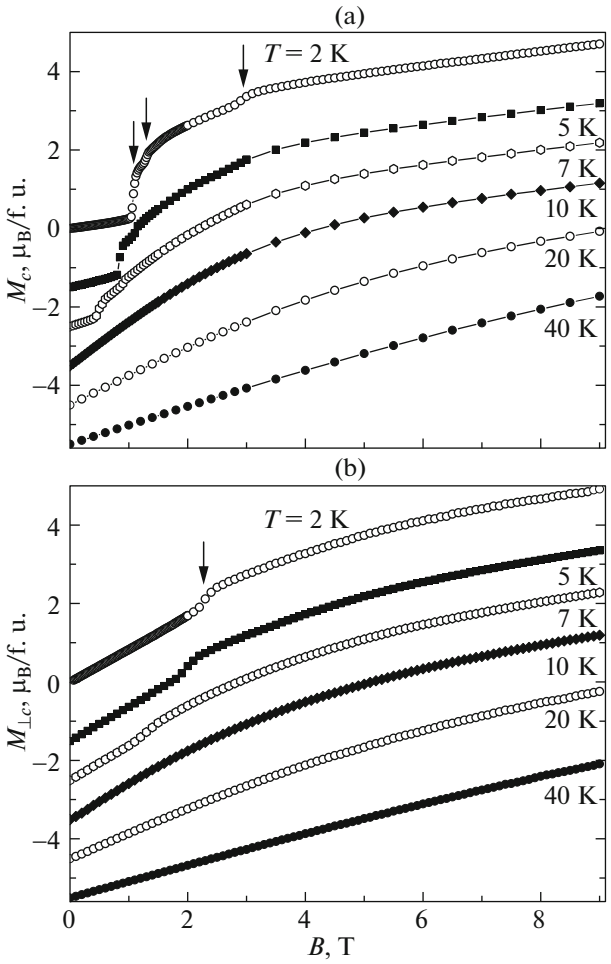

Fig. 2. Experimental magnetization curves $M_{c,\perp c}(B)$ for $Ho_{0.5}Nd_{0.5}Fe_3(BO_3)_4$ at (a) $\mathbf{B} \parallel \mathbf{c}$, (b) $\mathbf{B} \perp \mathbf{c}$ at $T = 2$ (0), 5 (−1.5), 7 (−2.5), 10 (−3.5), 20 (−4.5), and 40 (−5.5) K (in brackets are the coefficients of shifting along the vertical axis).

obtained at $T = 2$–40 K in magnetic fields directed along the trigonal axis ($\mathbf{B} \parallel \mathbf{c}$) (Fig. 2a) and in the basal plane ($\mathbf{B} \perp \mathbf{c}$). At $T < 10$ K, magnetization jumps can be clearly seen in the $M_c(B)$ curve and distinguished in $M \perp c(B)$ (Fig. 2b). At $T \geq 10$ K, the $M_{c,\perp c}(B)$ curves contain no anomalies. Thus, the temperature $T = 10$ K similar to the spin-reorientation transition temperature $T_{SR} \approx 9$ K [3] divides the investigated temperature range into two regions: with the $M_{c,\perp c}(B)$ anomalies at $T < 10$ K and without them at $T \geq 10$ K. This fact is confirmed by the field dependences of the magnetodielectric polarization $\varepsilon_a(B_a)$ at $T = 5$ and 10 K (Fig. 3a). One can see a significant difference between the $\varepsilon_a(B_a)$ behaviors upon temperature variation.

Of greatest interest is the $M_c(B)$ curve obtained at $T = 2$ K, which contains three magnetization jumps near $B \approx 1$, 1.3, and 2.9 T indicated by arrows in Fig. 2a. In addition, three jumps were observed upon switching-on and off the magnetic field; they can be clearly seen in the differential magnetic susceptibility curves (inset in Fig. 4). As the temperature increases, the third jump near 2.9 T becomes almost invisible already at $T = 5$ K, while the second jump is distinguished up to $T = 7$ K (near 0.9 T, see Fig. 2a). For the field lying in the basal plane, the only $M_c(B)$ anomaly at $T < 10$ K can be seen.

According to the results reported in [13], the initial low-temperature state of the $Ho_{0.5}Nd_{0.5}Fe_3(BO_3)_4$ magnetic subsystem at $B = 0$ is the angular state with

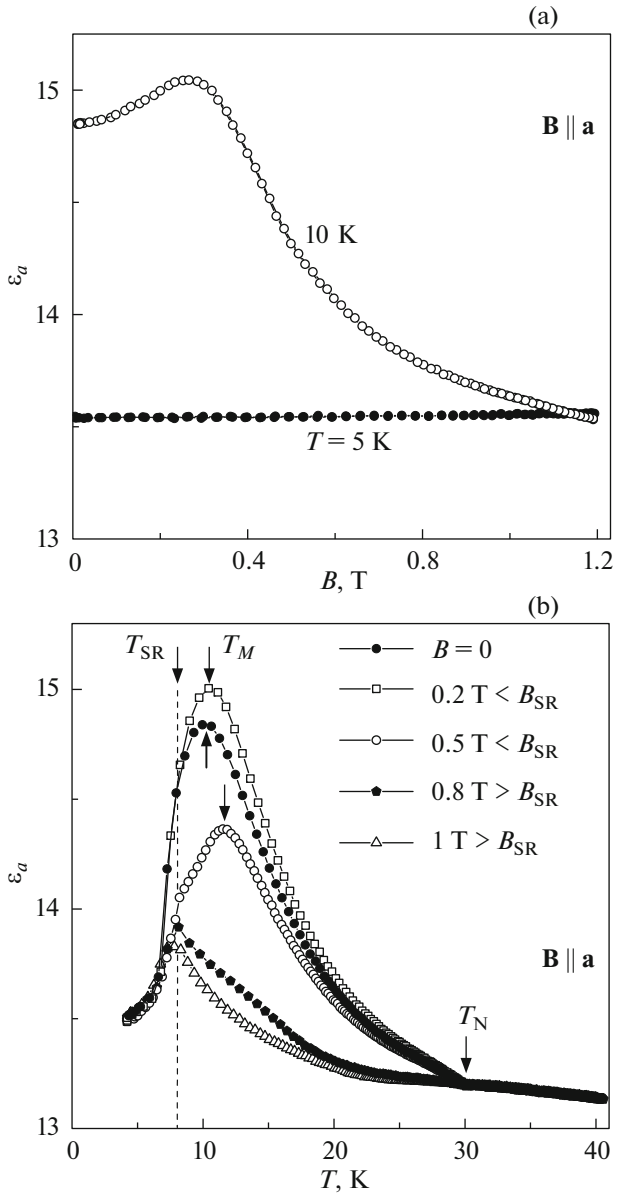

Fig. 3. Dependence of permittivity ε_a parallel the *a* axis of the $Ho_{0.5}Nd_{0.5}Fe_3(BO_3)_4$ crystal at a frequency of 10 kHz on (a) magnetic field $\mathbf{B} \parallel \mathbf{a}$ (at $T = 2$ K $< T_{SR}$ and $T = 10$ K $> T_{SR}$) and (b) temperature at $\mathbf{B} \parallel \mathbf{a}$. T_M is the temperature at which the $Ho_{0.5}Nd_{0.5}Fe_3(BO_3)_4$ domain structure transforms in the EP state at $\mathbf{B} \parallel \mathbf{a}$ and $B < B_{SR}$.

the iron magnetic moments deviated from the *c* axis (see the scheme in Fig. 1). Thus, the $M_{c,\perp c}(B)$ anomalies observed at $T < 10$ K (Fig. 2) are caused by the spin reorientation in the Fe subsystem from the initial angular phase (scheme *a* in Fig. 1) to the flop phase (scheme *d* at $\mathbf{B} \parallel \mathbf{c}$ and the analogous scheme at $\mathbf{B} \perp \mathbf{c}$).

The extensive calculations of the magnetic phases that can be implemented in $Ho_{0.5}Nd_{0.5}Fe_3(BO_3)_4$ at different orientations of the magnetic moments of the

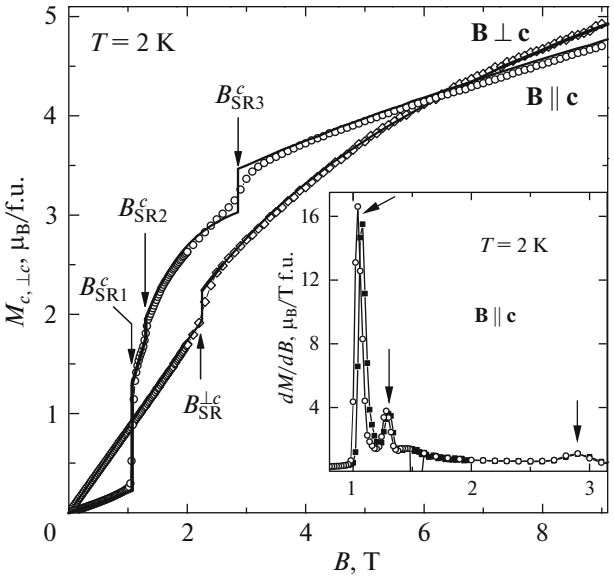

Fig. 4. Experimental (symbols) and calculated (lines) magnetization curves for $Ho_{0.5}Nd_{0.5}Fe_3(BO_3)_4$ at $\mathbf{B} \parallel \mathbf{c}$ and $\mathbf{B} \perp \mathbf{c}$ and $T = 2$ K. Inset: curves of differential magnetic susceptibility dM/dB upon switching-on (closed symbols) and off (open symbols) the magnetic field.

Ho, Nd, and Fe subsystems allowed us to attribute the three-step magnetization jump observed in the $M_c(B)$ curve at $T = 2$ K to the presence of intermediate states between the initial angular phase (scheme *a*) and flop phase (scheme *d*). The first, brighter $M_c(B)$ jump at B_{SR1} is related to an intermediate angular phase with a much larger angle of deviation of the Fe magnetic moments from the *c* axis ($\theta \approx 71°$) than in the initial phase ($\theta \approx 46.8°$) at B_{SR1} (scheme *c*), which is implemented in fields $B_{SR1} < B < B_{SR2}$. The second, weaker jump at B_{SR2} is due to the reorientation of the Fe magnetic moments from the intermediate state with $\theta_{SR1} \approx 71°$C to the state with $\theta_{SR2} \approx 72.5°$ (at B_{SR2}, scheme *c*). The third jump is caused by the spin reorientation from the intermediate state with $\theta_{SR2} \approx 72.5°$ to the flop phase ($\theta_{SR3} \to 90°$, scheme *c*) and accompanied by the reorientation along the field $\mathbf{B} \parallel \mathbf{c}$ of the magnetic moments of the Ho^{3+} and Nd^{3+} ion sublattices (scheme *d*). Thus, the transformation of the $Ho_{0.5}Nd_{0.5}Fe_3(BO_3)_4$ magnetic subsystem at $T = 2$ K with increasing field $\mathbf{B} \parallel \mathbf{c}$ includes the following stages relative to the variation in the angle of deviation of the Fe magnetic moments from the **c** axis (see scheme *c*): θ (at $B = 0$) $\to \theta_{SR1}$ (at B_{SR1}) $\to \theta_{SR2}$ (at B_{SR2}) $\to \theta_{SR3}$ (at B_{SR3}, the flop phase).

The possible magnetic field-induced intermediate states with a noncollinear antiferromagnetic structure result from the competition of the contributions of the Ho, Nd, and Fe subsystems to the total magnetic anisotropy of $Ho_{0.5}Nd_{0.5}Fe_3(BO_3)_4$ and Zeeman

energy. The magnetic anisotropy of the Nd and Fe subsystems stabilizes the EP magnetic structure. The holmium subsystem stabilizes the EA magnetic structure. As a result, at certain temperatures and fields, the iron magnetic moments can be oriented at angle θ to the *c* axis. As the magnetic field is increased, the balance of the contributions established in weak fields is violated; thus, at $T < T_{SR}$, in the field ranges of $B_{SR1} < B < B_{SR2}$ and $B_{SR2} < B < B_{SR3}$ the intermediate states with the Fe magnetic moments oriented at the larger angle θ to the *c* axis than in the previous state stabilize. Previously, in [24] and, then, in [25], the investigations of the $GdFe_3(BO_3)_4$ ferroborate undergoing the spin-reorientation transition made it possible to draw a conclusion about deviation of the Fe magnetic moments from the *c* axis by large angles changing with temperatures and magnetic fields. The possible implementation of the initial angular state was experimentally confirmed in the $Pr_xY_{1-x}Fe_3(BO_3)_4$ ferroborate in recent study [26]. Note also that the calculation based on the analogous mechanism of the magnetic subsystem transformation allowed us to explain the step anomalies in the $Nd_{1-x}Dy_xFe_3(BO_3)_4$ [7] and $Pr_xY_{1-x}Fe_3(BO_3)_4$ ferroborates [22]. The resulting magnetization parallel to the *c* axis in the temperature range of $T < 10$ K was calculated using the following formulas:

(i) In the initial angular phase at $0 \le B < B_{SR1}$ (scheme *b* in Fig. 1; $\theta_1 = 46.8°$ at $B = 0$):

$$M_c = \frac{1}{2}(M_1^{Fe}\cos(\theta_1) + M_2^{Fe}\cos(\theta_2) + 0.5(m_{2c}^{Ho} - m_{1c}^{Ho}) + 0.5(m_{2c}^{Nd} - m_{1c}^{Nd})). \quad (9)$$

II. In the intermediate phase at $B_{SR1} < B < B_{SR2}$ using formula (9) with $\theta_1 = \theta_{SR1} \approx 71°$ at B_{SR1} (scheme *c*).

III. In the intermediate phase at $B_{SR2} < B < B_{SR3}$ using formula (9) with $\theta_1 = \theta_{SR2} \approx 72.5°$ at B_{SR1} (scheme *c*).

IV. In the flop phase at $B > B_{SR3}$ and $\theta_1 = \theta_2 = \theta_{SR3}$ (scheme *d*):

$$M_{flop} = \frac{1}{2}(M_{1,2c}^{Fe} + 0.5m_{1,2c}^{Ho} + 0.5m_{1,2c}^{Nd}). \quad (10)$$

It can be seen in Fig. 4 that the calculation of the magnetization using formulas (9) and (10) allowed us to describe well the step anomalies in $M_c(B)$ at $T = 2$ K.

The temperature growth leads to smoothing of the magnetization jumps and the absence of an intermediate state distinguishable in the experimental curves in the field B_{SR3} at $T = 5$ and 7 K due to the implementation of the angular phase with the iron deviation angles close to the *ab* plane in fields of $B_{SR1} < B < B_{SR2}$. As a result, at $T = 5$ and 7 K, the only intermediate state with θ_{SR1} is implemented; then, in the field B_{SR2}, the transition to the flop phase occurs (scheme *d*). It is worth noting that, taking into account the established correlation between the magnetic, magnetoelectric, and magnetoelastic properties of ferroborates [4], the observed multiple features in the $M_c(B)$ curves at $T = 2$ and 5 K clarify the nature of jumps and kinks in the field dependence of polarization $P_a(H_c)$ of $Ho_{0.5}Nd_{0.5}Fe_3(BO_3)_4$ at $T = 5$ K from study [3] (Fig. 15b in [3]).

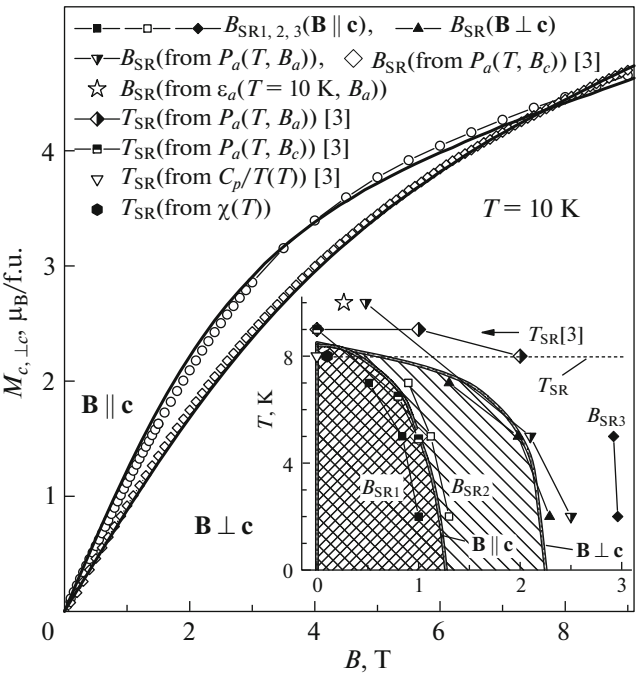

Fig. 5. Experimental (symbols) and calculated (lines) magnetization curves for $Ho_{0.5}Nd_{0.5}Fe_3(BO_3)_4$ at **B** ∥ **c** and **B** ⊥ **c** and $T = 10$ K. Inset: phase diagram based on our data and the data reported in [3]. The phase diagram from [3] is shown as regions with different hatches.

At $T > T_{SR}$, the $M_c(B)$ curves contain no visible anomalies (Fig. 2), the magnetic moments of the Ho, Nd, and Fe subsystems lie in the *ab* plane, and the calculation was made using formula (10). An example of the description of the experimental $M_c(B)$ curve from this range (at $T = 10$ K) is shown in Fig. 5.

When the trigonal $Ho_{0.5}Nd_{0.5}Fe_3(BO_3)_4$ crystal is magnetized in the basal *ab* plane in weak fields, all the three possible domains with the antiferromagnetic axes oriented at an angle of 120° to each other contribute to the magnetization (scheme *e* in Fig. 1). The $M_{\perp c}(B)$ curves at $B < B_{SR} \approx 2.3$ T at $T = 2$ K were calculated according to the approach used in the study of magnetization processes with regard to the possible existence of three types of domains in the EP $NdFe_3(BO_3)_4$ ferroborate [16] and $Sm_{0.7}Ho_{0.3}Fe_3(BO_3)_4$ ferroborate with the angular initial state [18]. The $M_c(B)$ anomaly at $T < T_{SR}$ (Figs. 1 and 4) is caused by the spin-reorientation transition from the initial angular phase (scheme *a* for $B = 0$ and scheme *e* in the projection

onto the *ab* plane at **B** ∥ **a**) to the flop phase. It can be seen that the calculated magnetization at temperatures below ($T = 2$ K $< T_{SR}$ (Fig.4)) and above ($T = 10$ K $> T_{SR}$ (Fig. 5)) the spin-reorientation transition describes the experiment sufficiently well.

The inset in Fig. 5 shows the phase diagram based on our experimental data and the data from the literature. The $Ho_{0.5}Nd_{0.5}Fe_3(BO_3)_4$ phase diagram from [3] is shown by the regions with different hatches. It can be seen that at **B** ∥ **c** and $T < T_{SR}$, according to [3], the field-induced phase transition boundary is located between the regions of stability of the intermediate phases at B_{SR1} and B_{SR2} (closed and open squares). According to the data from [3] obtained at **B** ∥ **a**, in the field lying in the basal plane at $T < T_{SR}$ [3], the phase transition boundary almost coincides with the transition fields (triangles) found by us in the $M_{\perp c}(B)$ curve. In addition, the phase diagram shows the T_{SR} data obtained from the $\chi_{c,\perp c}(T)$ and $C_p/T(T)$ curves [3] and $P_a(T, B)$ polarization curves [3].

It can be clearly seen from Fig. 1 and phase diagram (inset in Fig. 5) that the spin-reorientation transition field B_{SR} decreases with increasing temperature; i.e., as the temperature increases, the initial angular phase appears less stable, despite the increasing parallel susceptibility of the Fe subsystem. This $B_{SR}(T)$ dependence differs from the dependences for $RFe_3(BO_3)_4$ with R = Pr, Nd, Tb, and Dy, in which the field B_{SR} grew with temperature, as often happens in uniaxial antiferromagnets. Such a behavior of the $B_{SR}(T)$ dependence was observed in $HoFe_3(BO_3)_4$ [21] and is caused by the increasing similarity of the $M_c(B)$ curve measuring temperatures to the spin-reorientation transition temperature T_{SR}. As the temperature increases, the total effective anisotropy constant of the compound decreases from the R and Fe subsystems.

Figure 6 presents experimental and theoretical temperature dependences of susceptibility $\chi_{c,\perp c}(T)$. The experimental $\chi_{c,\perp c}(T)$ dependences measured at $B = 0.1$ T reveal a sharp drop of the susceptibility $\chi_c(T)$ and slight stepwise growth of $\chi_{\perp c}(T)$ near 8 K. The similar $\chi_a(T)$ behavior around 8 K (at $B = 0.1$T) and $\chi_c(T)$ behavior around 9 K (at $B = 0.02$ T) was observed in [3].

It was established that the angular phase with $\theta \approx 46.8°$ (at $T = 2$ K) makes it possible to explain and quantitatively describe the anomalies observed in the experimental $\chi_{c,\perp c}(T)$ curves near 8 K. A sharp decrease in $\chi_c(T)$ and a weaker jump in $\chi_{\perp c}(T)$ at $T \approx 8$ K are related to the change in the EP state for angular one with decreasing temperature. This spin-reorientation transition is caused by the different temperature dependences of the competing contributions of the rare-earth (Ho and Nd) and Fe subsystems to the total magnetic anisotropy of $Ho_{0.5}Nd_{0.5}Fe_3(BO_3)_4$. It can be seen that the calculation of the magnetization in a field

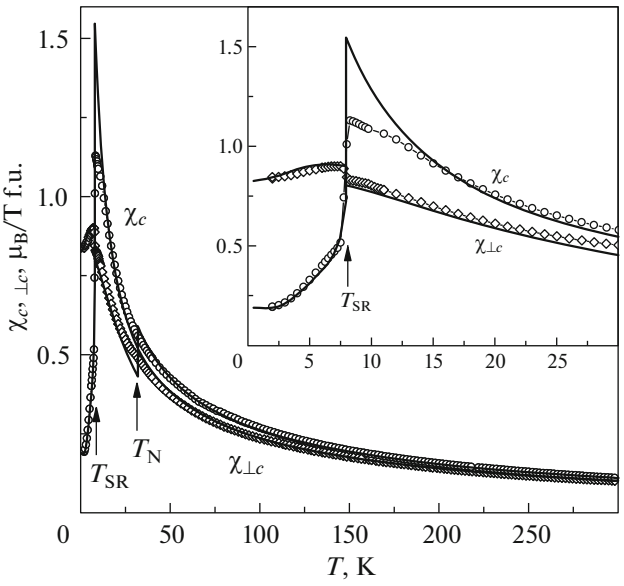

Fig. 6. Experimental (symbols) and calculated (lines) temperature dependences of the magnetic susceptibility of $Ho_{0.5}Nd_{0.5}Fe_3(BO_3)_4$ parallel (χ_c) and perpendicular ($\chi_{\perp c}$) to the trigonal axis at $B = 0.1$ T. Inset: low-temperature portion of the $\chi_{c,\perp c}(T)$ curve.

of $B = 0.1$ T in the initial angular phase ($T < T_{SR}$, scheme *b* for $\chi_c(T)$ and scheme *e* for $\chi_{\perp c}(T)$) and in the EP state ($T > T_{SR}$, scheme *d* for $\chi_c(T)$, and the analogous scheme for $\chi_{\perp c}(T)$) describes well the experimental curves (Fig. 6).

Note that the behavior of the experimental $\chi_{c,\perp c}(T)$ curves in the previously unexplored temperature range of $T = 20$–300 K confirms the earlier conclusion on the weakly anisotropic behavior of the susceptibility $\chi_{c,\perp c}(T)$ at $T > 20$ K, which was made in [13] on the basis of the calculations.

Figure 3b shows temperature dependences of the real part of permittivity ε_a parallel to the *a* crystal axis at a frequency of 10 kHz. It can be seen that the permittivity, which was almost invariable in the paramagnetic region, starts sharply growing below the Néel temperature. In this case, the temperature $T_{SR} \approx 8$ K determined from the specific heat [3] and susceptibility curves is located approximately in the middle of the range corresponding to the maximum decrease in $\varepsilon_a(T)$ at $B = 0$ and manifests itself in the form of a kink (at $B = 0.5$ T) and a peak (at $B = 0.8$ and 1 T) in the $\varepsilon_a(T)$ curve. The magnetic field applied in the basal plane leads to a small increase in the ε_a value with a decrease in temperature from T_N in a weak field of $B = 0.2$ T and, then, to the significant monotonic drop with increasing field. As a whole, the $\varepsilon_a(T)$ dependences contain two (at $B < B_{SR}$) or one (at $B > B_{SR}$) anomalies: at temperature T_M and, then, with a decrease in temperature near $T_{SR} \approx 8$ K. The $\varepsilon_a(B_a, T)$ measurements

in the frequency range from 10 kHz to 2 MHz showed that the frequency dependence of the permittivity is absent in the range from 10 to 200 kHz. The $\varepsilon_a(T)$ dependences of $Ho_{0.5}Nd_{0.5}Fe_3(BO_3)_4$ shown in Fig. 3b are consistent with the $\varepsilon_a(T)$ curves for $HoFe_3(BO_3)_4$ [3], which also contain two anomalies: a broad peak near 10 K (at T_M) and a sharp drop at $T_{SR} \approx 5$ K. Since the $\varepsilon_a(T)$ anomaly at T_M is observed in the field range of $B = 0$–0.5 T and at $T > T_{SR}$, and then vanishes at $B \geq 0.8$ T, this anomaly originates from the $Ho_{0.5}Nd_{0.5}Fe_3(BO_3)_4$ domain structure transformation in the EP state at $\mathbf{B} \parallel \mathbf{a}$. As was shown in [16, 18], at the field direction $\mathbf{B} \parallel \mathbf{a}$ in the EP ferroborates in the basal plane, the spin-flop transition occurs in one of three domains, which follow from the trigonal symmetry. The observed increase in the $\varepsilon_a(T)$ value near the temperature T_M in weak field $\mathbf{B} \parallel \mathbf{a}$ (see the curve at $B_a = 0.2$ T in Fig. 3b) and, then, the significant decrease in the $\varepsilon_a(T)$ value with a further increase in the field B_a correspond to the established nonmonotonic field dependence $\varepsilon_a(B_a)$ at $T = 10$ K (Fig. 3b), which reveals the $\varepsilon_a(B_a)$ growth in weak fields followed by an increase with increasing field.

It was established that the contribution of the R subsystem to the specific heat, which was calculated at CF parameters (8), as well as the components of this contribution associated with the Ho and Nd subsystems agree well with the experimental $C_p/T(T)$ curve for $Ho_{0.5}Nd_{0.5}Fe_3(BO_3)_4$ at $B = 0$ [3], where one can see a sharp peak near 8 K caused by the spin-reorientation transition. The calculated contribution of the R subsystem and the degree of its agreement with the experiment are similar to those reported in [13].

5. CONCLUSIONS

We experimentally and theoretically investigated the magnetic and magnetodielectric properties of $Ho_{0.5}Nd_{0.5}Fe_3(BO_3)_4$ with the competing Ho–Fe and Nd–Fe exchange couplings and obtained good agreement between the theory and experiment for the entire set of the measured characteristics. The single theoretical approach allowed us to determine the important parameters by comparing the calculated data with the experimental results.

The proposed variant of magnetization processes in magnetic fields of up to 9 T with the implementation of the angular magnetic structure made it possible to thoroughly analyze the behavior of the magnetic moments of the Ho, Nd, and Fe subsystems and describe the anomalies in the low-temperature magnetization curves $M_{c,\perp c}(B)$ at the transitions from the initial to intermediate phase (one or two, depending on temperature) and, then, to the flop phase.

We described the spontaneous spin-reorientation transition, which manifests itself as a bright anomaly in the $\chi_c(T)$ susceptibility curve and weaker pronounced in the $\chi_{\perp c}(T)$ curve. The calculated contribution of the rare-earth subsystem to the $Ho_{0.5}Nd_{0.5}Fe_3(BO_3)_4$ heat capacity reproduces the experimental results and elucidates the degree of responsibility of the rare-earth contribution components for the observed Schottky anomalies and the resulting heat capacity form.

ACKNOWLEDGMENTS

This study was supported by the Russian Foundation for Basic Research, project no. 17-52-45091 IND_a.

REFERENCES

1. A. K. Zvezdin, S. S. Krotov, A. M. Kadomtseva, G. P. Vorob'ev, Yu. F. Popov, A. P. Pyatakov, L. N. Bezmaternykh, and E. A. Popova, JETP Lett. **81**, 272 (2005).
2. E. A. Popova, D. V. Volkov, A. N. Vasiliev, A. A. Demidov, N. P. Kolmakova, I. A. Gudim, L. N. Bezmaternykh, N. Tristan, Yu. Skourski, B. Buechner, C. Hess, and R. Klingeler, Phys. Rev. B **75**, 224413 (2007).
3. R. P. Chaudhury, F. Yen, B. Lorenz, Y. Y. Sun, L. N. Bezmaternykh, V. L. Temerov, and C. W. Chu, Phys. Rev. B **80**, 104424 (2009).
4. A. M. Kadomtseva, Yu. F. Popov, G. P. Vorob'ev, A. P. Pyatakov, S. S. Krotov, K. I. Kamilov, V. Yu. Ivanov, A. A. Mukhin, A. K. Zvezdin, A. M. Kuz'menko, L. N. Bezmaternykh, I. A. Gudim, and V. L. Temerov, J. Low Temp. Phys. **36**, 511 (2010).
5. K.-C. Liang, R. P. Chaudhury, B. Lorenz, Y. Y. Sun, L. N. Bezmaternykh, V. L. Temerov, and C. W. Chu, Phys. Rev. B **83**, 180417(R) (2011).
6. Yu. F. Popov, A. M. Kadomtseva, G. P. Vorob'ev, A. A. Mukhin, V. Yu. Ivanov, A. M. Kuz'menko, A. S. Prokhorov, L. N. Bezmaternykh, and V. L. Temerov, JETP Lett. **89**, 345 (2009).
7. A. A. Demidov, I. A. Gudim, and E. V. Eremin, J. Exp. Theor. Phys. **114**, 259 (2012).
8. C. Ritter, A. Vorotynov, A. Pankrats, G. Petrakovskii, V. Temerov, I. Gudim, and R. Szymczak, J. Phys.: Condens. Matter **20**, 365209 (2008).
9. D. K. Shukla, S. Francoual, A. Skaugen, M. Zimmermann, H. C. Walker, L. N. Bezmaternykh, I. A. Gudim, V. L. Temerov, and J. Strempfer, Phys. Rev. B **86**, 224421 (2012).
10. A. K. Zvezdin, G. P. Vorob'ev, A. M. Kadomtseva, Yu. F. Popov, A. P. Pyatakov, L. N. Bezmaternykh, A. V. Kuvardin, and E. A. Popova, JETP Lett. **83**, 509 (2006).
11. E. A. Popova, A. N. Vasiliev, V. L. Temerov, L. N. Bezmaternykh, N. Tristan, R. Klingeler, and B. Buchner, J. Phys.: Condens. Matter **22**, 116006 (2010).
12. R. P. Chaudhury, B. Lorenz, Y. Y. Sun, L. N. Bezmaternykh, V. L. Temerov, and C. W. Chu, J. Appl. Phys. **107**, 09D913 (2010).
13. A. A. Demidov, Phys. B (Amsterdam, Neth.) 440, 73 (2014).

14. L. N. Bezmaternykh, V. L. Temerov, I. A. Gudim, and N. A. Stolbovaya, Crystallogr. Rep. **50**, S97 (2005).
15. I. A. Gudim, E. V. Eremin, and V. L. Temerov, J. Cryst. Growth **312**, 2427 (2010).
16. D. V. Volkov, A. A. Demidov, and N. P. Kolmakova, J. Exp. Theor. Phys. **104**, 897 (2007).
17. A. A. Demidov and D. V. Volkov, Phys. Solid State **53**, 985 (2011).
18. A. A. Demidov, I. A. Gudim, and E. V. Eremin, J. Exp. Theor. Phys. **115**, 815 (2012).
19. Yu. V. Gerasimova, S. N. Sofronova, I. A. Gudim, A. S. Oreshonkov, A. N. Vtyurin, and A. A. Ivanenko, Phys. Solid State **58**, 155 (2016).
20. A. A. Demidov, Extended Abstract of Doctoral Dissertation (Moscow State Univ., Moscow, 2016).
21. A. Pankrats, G. Petrakovskii, A. Kartashev, E. Eremin, and V. Temerov, J. Phys.: Condens. Matter **21**, 436001 (2009).
22. A. I. Pankrats, A. A. Demidov, C. Ritter, D. A. Velikanov, S. V. Semenov, V. I. Tugarinov, V. L. Temerov, and I. A. Gudim, J. Phys.: Condens. Matter **28**, 396001 (2016).
23. A. I. Pankrats, G. A. Petrakovskii, L. N. Bezmaternykh, and V. L. Temerov, Phys. Solid State **50**, 79 (2008).
24. S. A. Kharlamova, S. G. Ovchinnikov, A. D. Balaev, M. F. Thomas, L. S. Lyubutin, and A. G. Gavriliuk, J. Exp. Theor. Phys. **101**, 1098 (2005).
25. K. V. Frolov, I. S. Lyubutin, E. S. Smirnova, O. A. Alekseeva, I. A. Verin, V. V. Artemov, S. A. Kharlamova, L. N. Bezmaternykh, and I. A. Gudim, J. Alloys Compd. **671**, 545 (2016).
26. C. Ritter, A. I. Pankrats, A. A. Demidov, D. A. Velikanov, V. L. Temerov, and I. A. Gudim, Phys. Rev. B **91**, 134416 (2015).

Translated by E. Bondareva